How to cite:
doi.org/10.1002/anie.202305299

Nanostructures

Yolk-Shell Nanostars@Metal Organic Frameworks as Molecular Sieves for Optical Sensing and Catalysis

Tolga Zorlu, I. Brian Becerril-Castro, Begoña Puertolas, Vincenzo Giannini, Miguel A. Correa-Duarte, and Ramon A. Alvarez-Puebla**

Abstract: Hybrid composites between nanoparticles and metal organic frameworks (MOFs) have been described as optimal materials for a wide range of applications in optical sensing, drug delivery, pollutant removal or catalysis. These materials are usually core-shell single- or multi-nanoparticles, restricting the inorganic surface available for reaction. Here, we develop a method for the preparation of yolk-shells consisting in a plasmonic gold nanostar coated with MOF. This configuration shows more colloidal stability, can sieve different molecules based on their size or charge, seems to show some interesting synergy with gold for their application in photocatalysis and present strong optical activity to be used as SERS sensors.

[*] T. Zorlu, I. B. Becerril-Castro, Prof. R. A. Alvarez-Puebla
Department of Physical and Inorganic Chemistry,
Universitat Rovira i Virgili
Tarragona (Spain)
E-mail: ramon.alvarez@urv.cat

T. Zorlu, Dr. B. Puertolas, Prof. M. A. Correa-Duarte
Department of Physical Chemistry,
Universidade de Vigo
36310 Vigo (Spain)
and
CINBIO,
Universidade de Vigo
36310 Vigo (Spain)
E-mail: macorrea@uvigo.gal

Prof. V. Giannini
Instituto de Estructura de la Materia (IEM),
Consejo Superior de Investigaciones Científicas (CSIC)
28006 Madrid (Spain)
and
Technology Innovation Institute
9639 Masdar City, Abu Dhabi (United Arab Emirates)
and
Centre of Excellence ENSEMBLE3 sp. z o.o.
Wolczynska 133, 01-919 Warsaw (Poland)

Prof. R. A. Alvarez-Puebla
ICREA—Institució Catalana de Recerca i Estudis Avançats
08010 Barcelona (Spain)

Introduction

Composite materials comprising plasmonic cores coated with inorganic oxides or polymers are not new.[1] These materials have been extensively engineered to improve colloidal stability, restrict the reactivity, and to impart physical and/or chemical selectivity. Conversely, formats of these composites range from single particles[2] to several aggregates[3] or semi-isolated particles[4] coated with the desired material. Additionally, composites can be obtained as regular core–shell[1] or yolk-shell[5] materials. These composites have found applications in fields such as sensing,[6] drug delivery[7] and catalysis,[8] among others. However, these coatings commonly present a heterogeneous collection of pore sizes, a critical parameter for these applications.

Metal organic frameworks (MOFs) have shown outstanding performance in various strategic applications such as separation, catalysis or sensing and drug delivery systems.[9] The strength of MOF-based materials arise of their structure-dependent regular network of voids (with diameters up to 6 nm),[10] which are defined by inorganic cations interconnected by polydentate organic ligands. Since the late 1990s intense synthetic efforts have been devoted to report novel MOFs (over 20,000 structures) in terms of crystal size, porosity, geometry, and functionality.[9a,11] More recently, composites containing plasmonic nanoparticles (NPs) had been prepared in a variety of morphologies for a diversity of applications as sensors,[12] catalyst[13] and drug delivery scaffolds.[14] These composites combine the optical/catalytic properties of the plasmonic nanoparticles with the structural properties of the MOFs which, together with the high surface area due to a vast porosity of a very homogeneous distribution,[15] may offer additional chemical selectivity based on the ligands used in the coordination of the metal.[16]

As other hybrid materials NP-MOF composites can be prepared coating single or multiple (isolated and aggregated) nanoparticles.[17] However, these core–shell approaches notably restrict the availability of the plasmonic surfaces limiting their capacity to interact with the target analytes or molecular substrates and their storage capacity to be used as drug delivery systems.[5]

Herein, we demonstrate the possibility of confining single gold nanostars into a water-soluble MOF (ZIF67) that can be recoated through epitaxial growth with a water-insoluble MOF (ZIF8) to create a yolk-shell. This method preserves the nanostar structure, and thus the optical

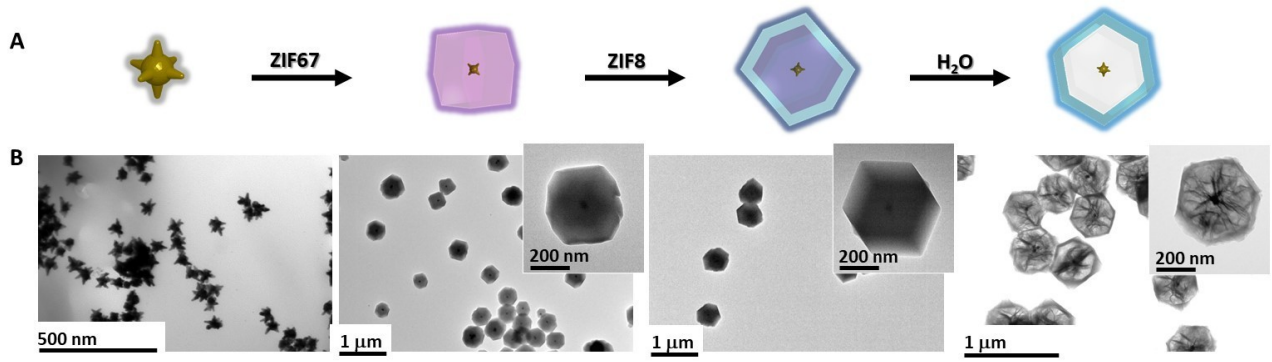

Figure 1. (A) Conceptual Scheme for the preparation of NSt-ZIF67 core-shells and NSt-ZIF8 yolk-shells and (B) representative TEM images of the different materials.

properties. This cannot be achieved by using other method such as the use of copper oxide as sacrificial material,[18] or the selective etching with tannic acid[9b] due to the reshaping of the spiked particles. Optical performance as well as retention kinetics in multianalyte experiments and plasmonic catalysis are also studied.

Results and Discussion

Similar (structurally) zeolitic imidazolate frameworks (ZIF) MOFs present different physicochemical properties. For example, the cobalt (II) and zinc (II) derived ZIFs ($[Zn(2\text{-methylimidazole})_2]_n$, ZIF8 and $[Co(2\text{-methylimidazole})_2]_n$, ZIF67) consist in tetrahedral crystals that share a quasi-identical sodalite topology. However, while ZIF67 is soluble in water, ZIF8 is much more resistant, both at room temperature (Figure S1). Thus, taking advantage of this property, it is possible to produce yolk-shells consisting in single gold nanostars (NSt) coated of ZIF8 (Figure 1A). Gold nanostars of 70 nm (tip-to-tip) were produced though a seed-mediated method (Figure 1B and S2).[19] These nanoparticles were selected as they are single-particle electromagnetic hot spots in the near IR.[20] Then, preparation of yolk-shell structures was achieved by initially coating the nanostars with ZIF67, followed by the growth of the ZIF8 to create a ZIF67/ZIF8 double shell. NSt-ZIF8 yolk-shell can be then spontaneously prepared by immersing the previous material in water and sonicating for 24 hours (Figures 1B, S3).[21] Notably, while the violet solution of the core-shell particles rapidly turns to colorless in few minutes, in the case of yolk-shell, the presence of the outer ZIF8 layer delays the ZIF67 dissolution (Figure S4). For the nanostars after the MOF deposition or remotion we did not detect any morphological change Figure S2).

To assess the composition of the produced materials, energy dispersive X-ray analysis (EDX) was carried out in a high-resolution TEM. As shown in Figure 2, core-shell structures present signals of gold and cobalt that correspond to the Au NSts and the coating ZIF67, respectively. In the case of the intermediate NSt-ZIF67/ZIF8 composites, an additional signal arises at the outer surface due to the zinc

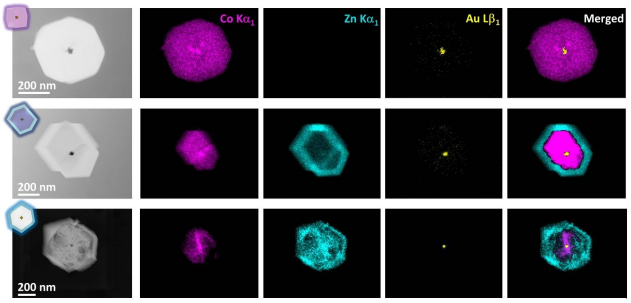

Figure 2. High resolution TEM images and EDX analysis of the AuNSt-ZIF67 and AuNSt-ZIF67/ZIF8 core-shell and the AuNSt-ZIF8 yolk-shell.

ions of the ZIF8. Upon dissolution of the inner ZIF67 structure, the Zn signal remains in the outer shell while traces of the cobalt signal remain. This reminiscent signal can be attributed to the spontaneous formation of some layered cobalt oxides as this cation detaches from the MOF,[21c] as also indicated by the TEM images (Figure 1B and S3)

Powder x-ray diffraction patterns of the samples (Figure 3A) exhibit sharp bands that correspond to the sodalite structures of crystalline ZIF8 and ZIF67 in both core and Yolk shell structures.[22] The absence of any other signals demonstrates the phase purity of the MOFs but also the epitaxial growth of ZIF8 on ZIF67. This is expected due to the similar sizes of the unit cell for ZIF8 ($a=b=c=$ 16.9910 Å)[23] and ZIF67 ($a=b=c=16.9589$ Å).[24] The structure remains unchanged after the removal of the ZIF67 in water. The nitrogen adsorption isotherms (Figure 3B) of the core and yolk-shells show the typical reversible type I isotherm, as previously observed for pure ZIF8 and ZIF67 crystals.

For both, the amount of adsorbed nitrogen rapidly increases at low pressures, indicating the existence of micropores.[25] The Brunauer-Emmett-Teller (BET) analysis of the isotherms indicates surface areas over 1700 and 1100 $m^2 g^{-1}$ for the core and the yolk-shell structures, respectively. These values also fall within the common range reported for pristine ZIF particles.[26] The difference in the

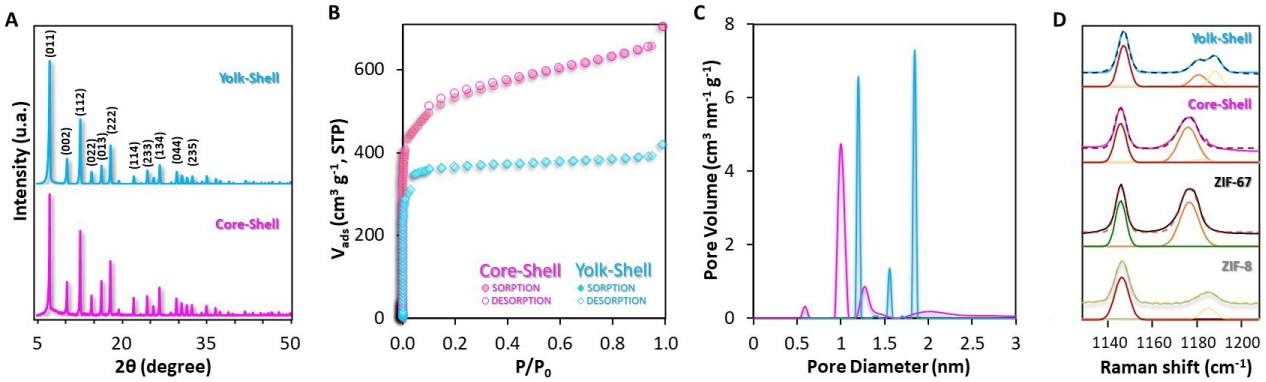

Figure 3. (A) X-ray power diffraction, (B) nitrogen sorption isotherms (77 K), (C) Barrett-Joyner-Halenda (BJH) pore size analysis and (D) Raman spectroscopy for the AuNt-ZIF67 core-shells and the AuNSt-ZIF8 yolk-shells.

surface area of the both structures is related to the shell thickness of the composites. While the AuNSt-ZIF67 core-shell particles exhibit a continuous shell of 160 nm, the yolk-shell show an outer shell of only 50 nm. Porosity, derived from the isotherms through the Barrett–Joyner–Halenda (BJH) pore size analysis, also shows different distributions for core and Yolk shells. While AuNSt-ZIF67 core-shell exhibits most of its porosity at 1 nm, with small contributions at 0.6 and 1.3 nm, pore distribution of AuNSt-ZIF8 Yolk shell shows larger pores, at 1.2 and 1.9 nm, with a smaller contribution at 1.6 nm. Although ZIF67 and ZIF8 present similar pore distributions in large crystals the epitaxial growth of ZIF8 on ZIF67, and the posterior removal of ZIF67 have two main effects in the structure of the Yolk shell. First, the growth, by itself, of a MOF on the surface of a nanoparticle slightly enlarge the pores as the shell grows.[27] Second, the removal of the sacrificial ZIF67 increases the flexibility of the ZIF8 Yolk shell due to the removal of the mechanical support imparted by ZIF67. Finally, Raman spectroscopy was carried out on the composites in solid phase (Figure 3D and S5). In the case of the pure ZIF crystals, the vibrational spectra are dominated by the characteristic vibrational modes of the zeolitic imidazolate frameworks (imidazole ring puckering, 685 cm^{-1}; the CN stretching, 1146 cm^{-1} and the CCH waging, 1460 cm^{-1}).[14] However, a detailed observation of the area between 1100 and 1200 cm^{-1} (Figure 3D) indicates a slight difference (1178 and 1187 cm^{-1} for ZIF67 and ZIF8, respectively) in the band assigned to the CN stretching plus the NH wagging,[28] which is affected by the nature of the coordinated metal. This vibrational detail can be exploited to gain information about the composition of the composite materials. The fine deconvolution of the CN stretching, and CN stretching plus the NH wagging bands clearly shows that while the AuNSt-ZIF67 core-shell can be deconvoluted in just two bands, three bands are necessary for the Yolk shell. Considering the low contribution of the 1178 cm^{-1} ZIF67 signal (which is similar to the CN stretching in the ZIF67 pure crystal) and the distance to the surface of ZIF8 (much distant than ZIF67, with the subsequent less SERS effect in the intensity of its spectrum) it becomes clear that the presence of Co^{II} is reminiscent in the yolk shell.

Figure 4A shows the experimental and simulated optical response for AuNSts, AuNSt-ZIF67 core-shell and AuNSt-ZIF8 yolk-shell. The spectra simulated for the nanostar and the Yolk shell present a good agreement with the experimental results. However, the theoretical spectrum of the core-shell shows slight differences compared to the experimental result, which can be attributed to the imaginary part of the dielectric constant of the MOF, which we assumed to be zero in the simulations to make the calculation treatable.[29] This approximation gives sharper theoretical resonances compared with the experiments. Notably, the removal of the sacrificial ZIF67 shell is illustrated by the disappearance of the absorption band around 590 nm, which is present in the core-shell system but not in the yolk-shell (Figure S6A shows the spectrum of pristine ZIF for completion's sake). Electric near field (Figure 4B) shows similar enhancements for the single NSt and the Yolk shell system; this is expected because the ZIF8 slightly attenuates the incident light that reaches the nanostars, thus slightly diminishing the intensity of the near-field enhancement. This explanation is corroborated by a simulation of an empty ZIF8 (Figure S6B) which shows that the shell alone acts as a scattered, thus reducing the intensity of the light incoming to the nanostar. On the other hand, results for the core-shells show a lower enhancement as compared with stars and Yolk shells. This is due to the proximity of the ZIF67 to the plasmonic structure which, in fact, increases the local refractive index (of the liquid solution); this implies a redshift of the resonances and dumps the enhancement as the plasmon resonance.

To test for the optical enhancing properties for SERS,[30] the different materials, nanostars, core and yolk-shells were exposed to 4 different analytes: 2-naphthalenethiol (NAT), benzenethiol (BT), 4-mercaptobezoic acid (MBA) and 4-aminobenzenethiol (ABT). The selected analytes were added to the plasmonic solutions to set a final concentration of 10^{-6} M. Spectra were recorded after 30 minutes, time that is usually enough for the chemisorption reaction to be completed (Figure 4C).[31] Notably, NAT and BT yield

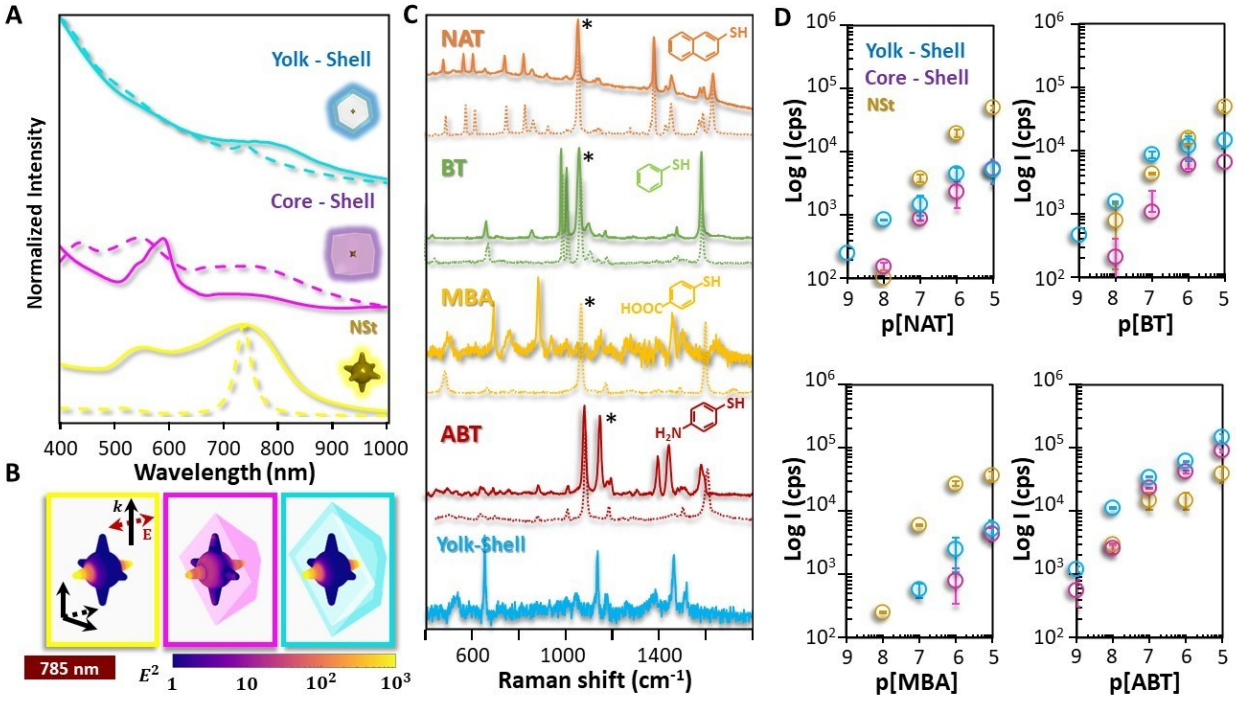

Figure 4. (A) Experimental (solid line) and calculated (dashed) extinction and (B) local electric field distribution at 785 nm for a gold nanostar and its core-shell composite with ZIF67 and Yolk shell composite with ZIF8. (C) SERS spectra of micromolar solution of 2-naphthalenethiol (NAT), benzenethiol (BT), 4-mercaptobezoic acid (MBA) and 4-aminobenzenethiol (ABT) on the nanostars (dashed lines) and Yolk shells (solid lines). The intensity of each pair of spectra (bare nanostar and Yolk shell) with the same analyte is normalized to the one with higher intensity. For reference, the spectrum of the Yolk shell solution without analyte is also shown. Marked bands (asterisk) were used to set the detection limits. (D) Comparison of the intensities for each analyte on the different substrates at different concentrations after 30 minutes of addition.

strong signals on all substrates. MBA, however, only produces remarkable intensity on the bare nanostars, with no evidence of its presence on both core and Yolk shells. ABT shows only its characteristic spectrum on the nanostars, while in the case of the composite materials the signals obtained can be ascribed to 4,4-dimercaptoazobenzene (DMAB) a product derived from the plasmonic driven catalytical dimerization of ABT.[32] Further, for all the analytes, but ABT (or DMAB), SERS intensity on nanostars resulted consistently better than that obtained on the composite materials. Notwithstanding, the study of the detection limits (Figure 4D) indicates that while at high concentrations of NAT, BT and ABT the SERS intensity on nanostars prevails, while at lower concentrations signals provided by the Yolk shells are remarkably higher. This fact fully agrees with the literature, which often considers the plasmonic nanoparticles coated with MOFs as an example of optical accumulators.[12b,33] Notably, in the case of MBA the signal is always higher on nanostars. These results suggest some kind of inhibition of the MOF composites to adsorb these molecules. Thus, to further investigate this point, we designed a set of experiments based on the adsorption kinetics of single probes as compared with the same probes in the presence of the rest (Figure 5 and S7). For that, colloidal solutions were set at pH 7.8 with analyte concentrations of 10^{-6} M (either just one or all the analytes). The examination of the temporal response of the analyte spectral intensities reveals an exponential rise to maximum curve. Thus, when the analyte collides with the adsorbent, it will chemically bind to the plasmonic surface, or it will return to the aqueous phase, which indicates a pseudo-first-order chemical kinetics:[12a,34]

$$q_t = q_{eq}\left(1 - e^{-kt}\right) \quad (1)$$

where q_t is the amount adsorbed by the adsorbent at any time; q_{eq}, the adsorption capacity at the equilibrium (or amount adsorbed by the adsorbent at the equilibrium); k, rate constant and t, the time of reaction. Assuming that, in a liquid colloidal suspension without aggregation, the SERS intensity (I) is equivalent to the amount adsorbed this equation (equation 1) can be used to fit the kinetic data of the probes to obtain the rate constants.[35] To give quantitative comparison between different analytes, the kinetic models require to take into consideration the particular cross-section of the given analyte to the applied spectroscopic technique. Although these values are scarce, the chemical structures studied here are very similar implying a similar cross-section.

To give an interpretation of the kinetic results, Zeta potential of the colloidal solutions was measured resulting in values of −29, 25 and 11 mV for the nanostars, core and yolk shells, respectively. Conversely, molecular size of the analytical probes was calculated by using DFT at the

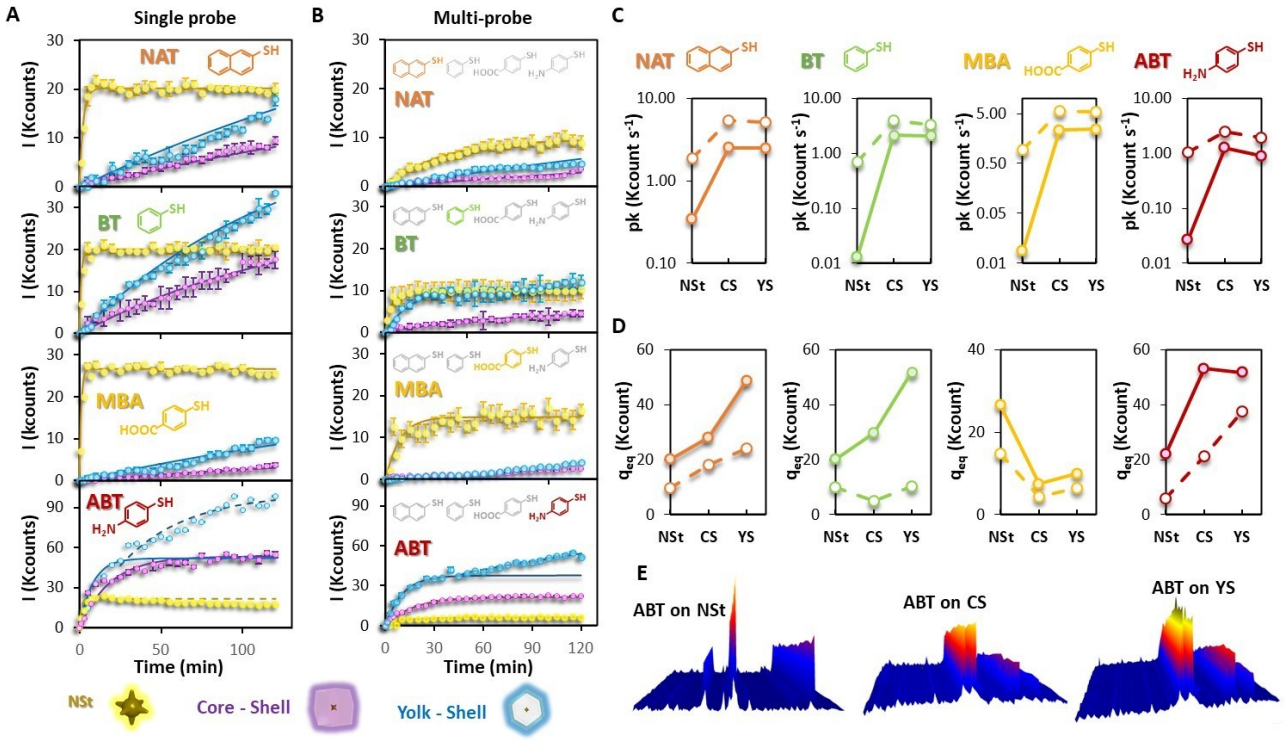

Figure 5. Adsorption kinetics of micromolar solutions 2-naphthalenethiol (NAT), benzenethiol (BT), 4-mercaptobezoic acid (MBA) and 4-aminobenzenethiol (ABT) on the nanostars (NSt), core (CS) and Yolk shells (YS), (A) as single probes and (B) in a mixture containing all the molecules. (C) Rate constant for the kinetics and (D) adsorption capacity at the equilibrium (solid line, single probe; dashed line, multiprobe). (E) Three-dimensional representation of the kinetic adsorption of ABT on nanostars and on the core and Yolk shells.

B3LYP 6-311G (d,p) level of theory (Figure S8) resulting in a molecular volume tendency of NAT > MBA > ABT > BT. Since the core-shell material exhibit most of its porosity at 1 nm, while the yolk-shell show larger pores, at 1.2 and 1.9 nm, the introduction of the analytes into the MOF is expected. However, it is clear that larger analytes will be hindered as compared with smaller ones. In general, all the analytes are adsorbed faster (and in a larger quantity) when they are alone as compared when they are in the mixture between themselves. This fact is expected as single probes have not competition with other adsorbates. Further, although nanostars tend to adsorb faster (Figure 5C), adsorption capacity is maximized in Yolk shells (Figure 5D). This indicates that the sieving layer, provided by the MOF, restricts the pass of the analyte, but favor the accumulation on the plasmonic surface once into the shell as expected in an optical accumulator.[6] Notably, this effect is more noticeable in the case of Yolk shells as they are hollow and their plasmonic surface much more available. Related with this, it is important to mention that the MOF coating also increases colloidal stability. For example, after 2 h, nanostars tend to precipitate when the analyte is ABT (Figure S9) while both composites remain stable. Considering the differences between analytes, it can be stated that for neutral molecules such as NAT and BT size is an important parameter as, although it does not affect the retention capacity, it slows the sorption process for the larger entities. On the other hand, analyte charge is a key factor. At pH 7.8 all the analytes but MBA are neutral. At this pH, MBA is ionized as mercaptobenzoate (i.e., marked with an explicit negative charge). Notwithstanding, this molecule is readily adsorbed on nanostars, which are eminently negative, but not in core of Yolk shells, which exposes a positively charged surface. This behavior results very likely from an extraordinary electrostatic affinity between the MOF and the MBA which clogs the pores or considering the volume of the pore at least a partial blockage.[36] This phenomenon is more remarkable as the MOF material increases[37] as illustrated in in the smaller retention capacity of core-shells as compared with Yolk shells. This clogging or fouling process does not affect the rest of analytes in the multiprobe experiments. If it is true that in such experiments, both rate constant and retention capacity decrease as compared with those of single probe, the decrease of kinetic constants and the retention capacity is very likely derived of the competence between the different probes.

The sorption of ABT shows a different behavior as compared with the rest of the probes (Figure 5E). ABT retention in nanostars shows the typical SERS spectrum of such molecule during all the acquisition time until aggregation. Notwithstanding, when measured either on core or Yolk shells, the resulting spectrum is no longer ABT but 4,4-dimercaptoazobenzene (DMAB). The dimerization of this molecule is an example of plasmonic catalysis and has been described upon illumination of plasmonic sols in an excess of ABT,[38] in lower ABT concentrations when

plasmonic nanoparticles are functionalized with platinum[32] or when a ABT monolayer is deposited in a plasmonic electrode.[39] Briefly, ABT oxidizes to DMAB by losing 2e (or gaining 2 holes). Oxidation of ABT on gold surfaces is a thermodynamically nonspontaneous reaction. Plasmon excitation and subsequent decay in metal nanoparticles create hot electrons and hot holes with an energy distribution above and below the Fermi level. When the lowest unoccupied molecular orbital (LUMO) or the highest occupied molecular orbital (HOMO) energies of the molecules are within the energy distribution, hot charge carriers are allowed to transfer to the molecules, leading to the reduction or oxidation of the molecules. Herein, ZIF8 increases the local concentration of ABT onto the gold nanostars favoring its subsequent dimerization. As observed in Figure 5E, this transformation occurs in both type of nanostructures, i.e., core- and yolk-shells. However, in the case of the core-shells, it happens to a lower extent owing to the smaller available plasmonic surface area allowed by the compact thick shell of ZIF and its smaller hollow volume. Thus, the MOF layer is acting as an active molecular sieve that can selectively start a well described plasmonic reaction.

Conclusion

In summary, we described a simple and effective synthetic method for the fabrication of single gold nanostars encapsulated into hollow ZIF8 Yolk shells. The resulting materials are characterized by three main features: (i) the electromagnetic response of isolated gold nanostars even in concentrated solution or even cast on surface; (ii) the homogeneous porous distribution characteristic of MOF materials; and, (iii) the availability of a large volume between the plasmonic core and the sieving shell that can be exploited for optical accumulation, catalysis or drug storage. These materials are more colloidally stable than their counterparts without coating, can sieve different molecules based on their size or charge, seems to show some interesting synergy with gold for their application in photocatalysis and present strong optical activity to be used as SERS sensors. Further, the dependence of the SERS signal with time can be also used to design advanced analytical applications based in the adsorption time (kinetic control) or the stability (thermodynamic stability).

Acknowledgements

This research was supported by the projects PID2020-120306RB-I00 and PID2020-113704RB-I00 (funded by MCIN/AEI/10.13039/501100011033), PDC2021-121787-I00 (funded by MCIN/AEI/10.13039/501100011033 and European Union Next Generation EU/PRTR), 2017SGR883 (funded by Generalitat de Cataluña) and 2021PFR-URV-B2-02 (funded by Universitat Rovira I Virgili). Xunta de Galicia (Centro Singular de Investigación de Galicia - Accreditation 2019–2022 ED431G 2019/06, IN607 A 2018/5 and ED431 C 2021/45), and European Union-ERDF (0712_ACUINANO_1_E, and 0624_2IQBIONEURO_6_E, and Interreg Atlantic Area NANOCULTURE 1.102.531). The ENSEMBLE3 project (GA No. MAB/2020/14) Foundation for Polish Science-European Union (GA.No. 857543).

Conflict of Interest

The authors declare no conflict of interest.

Data Availability Statement

The data that support the findings of this study are available from the corresponding author upon reasonable request.

Keywords: Metal Organic Frameworks · Optical Sensing · Plasmonic Composites · SERS · Yolk Shells

[1] R. Ghosh Chaudhuri, S. Paria, *Chem. Rev.* **2012**, *112*, 2373–2433.
[2] L. M. Liz-Marzán, M. Giersig, P. Mulvaney, *Langmuir* **1996**, *12*, 4329–4335.
[3] M. Sanles-Sobrido, W. Exner, L. Rodrífguez-Lorenzo, B. Rodríguez-González, M. A. Correa-Duarte, R. A. Álvarez-Puebla, L. M. Liz-Marzan, *J. Am. Chem. Soc.* **2009**, *131*, 2699–2705.
[4] I. Pastoriza-Santos, C. Kinnear, J. Pérez-Juste, P. Mulvaney, L. M. Liz-Marzán, *Nat. Rev. Mater.* **2018**, *3*, 375–391.
[5] M. Blanco-Formoso, A. Sousa-Castillo, X. Xiao, A. Mariño-Lopez, M. Turino, N. Pazos-Perez, V. Giannini, M. A. Correa-Duarte, R. A. Alvarez-Puebla, *Nanoscale* **2019**, *11*, 21872–21879.
[6] R. A. Álvarez-Puebla, R. Contreras-Cáceres, I. Pastoriza-Santos, J. Pérez-Juste, L. M. Liz-Marzán, *Angew. Chem. Int. Ed.* **2009**, *48*, 138–143.
[7] R. Bardhan, S. Lal, A. Joshi, N. J. Halas, *Acc. Chem. Res.* **2011**, *44*, 936–946.
[8] A. Sousa-Castillo, J. R. Couceiro, M. Tomás-Gamasa, A. Mariño-López, F. López, W. Baaziz, O. Ersen, M. Comesaña-Hermo, J. L. Mascareñas, M. A. Correa-Duarte, *Nano Lett.* **2020**, *20*, 7068–7076.
[9] a) H. Furukawa, K. E. Cordova, M. O'Keeffe, O. M. Yaghi, *Science* **2013**, *341*, 1230444; b) X. Deng, S. Liang, X. Cai, S. Huang, Z. Cheng, Y. Shi, M. Pang, P. A. Ma, J. Lin, *Nano Lett.* **2019**, *19*, 6772–6780.
[10] P. Li, N. A. Vermeulen, C. D. Malliakas, D. A. Gómez-Gualdrón, A. J. Howarth, B. L. Mehdi, A. Dohnalkova, N. D. Browning, M. O'Keeffe, O. K. Farha, *Science* **2017**, *356*, 624–627.
[11] N. Stock, S. Biswas, *Chem. Rev.* **2012**, *112*, 933–969.
[12] a) L. B. T. Nguyen, Y. X. Leong, C. S. L. Koh, S. X. Leong, S. K. Boong, H. Y. F. Sim, G. C. Phan-Quang, I. Y. Phang, X. Y. Ling, *Angew. Chem. Int. Ed.* **2022**, *61*, e202207447; b) C. Koh, O. Sim, S. X. Leong, S. K. Boong, C. R. C. Chong, X. Y. Ling, *ACS Mater. Lett.* **2021**, *3*, 557–573.
[13] J. Liu, L. Chen, H. Cui, J. Zhang, L. Zhang, C. Y. Su, *Chem. Soc. Rev.* **2014**, *43*, 6011–6061.
[14] C. Carrillo-Carrión, R. Martínez, M. F. Navarro Poupard, B. Pelaz, E. Polo, A. Arenas-Vivo, A. Olgiati, P. Taboada, M. G. Soliman, Ú. Catalán, S. Fernández-Castillejo, R. Solà, W. J.

Parak, P. Horcajada, R. A. Alvarez-Puebla, P. del Pino, *Angew. Chem. Int. Ed.* **2019**, *58*, 7078–7082.
[15] H. Furukawa, N. Ko, Y. B. Go, N. Aratani, S. B. Choi, E. Choi, A. O. Yazaydin, R. Q. Snurr, M. O'Keeffe, J. Kim, O. M. Yaghi, *Science* **2010**, *329*, 424–428.
[16] L. He, Y. Liu, J. Liu, Y. Xiong, J. Zheng, Y. Liu, Z. Tang, *Angew. Chem. Int. Ed.* **2013**, *52*, 3741–3745.
[17] C. Wiktor, M. Meledina, S. Turner, O. I. Lebedev, R. A. Fischer, *J. Mater. Chem. A* **2017**, *5*, 14969–14989.
[18] C.-H. Kuo, Y. Tang, L.-Y. Chou, B. T. Sneed, C. N. Brodsky, Z. Zhao, C.-K. Tsung, *J. Am. Chem. Soc.* **2012**, *134*, 14345–14348.
[19] S. Barbosa, A. Agrawal, L. Rodriguez-Lorenzo, I. Pastoriza-Santos, R. A. Alvarez-Puebla, A. Kornowski, H. Weller, L. M. Liz-Marzan, *Langmuir* **2010**, *26*, 14943–14950.
[20] I. B. Becerril-Castro, I. Calderon, N. Pazos-Perez, L. Guerrini, F. Schulz, N. Feliu, I. Chakraborty, V. Giannini, W. J. Parak, R. A. Alvarez-Puebla, *Anal. Sens.* **2022**, *2*, e202200005.
[21] a) J. Yang, F. J. Zhang, H. Y. Lu, X. Hong, H. L. Jiang, Y. Wu, Y. D. Li, *Angew. Chem. Int. Ed.* **2015**, *54*, 10889–10893; b) C. Rösler, A. Aijaz, S. Turner, M. Filippousi, A. Shahabi, W. Xia, G. Van Tendeloo, M. Muhler, R. A. Fischer, *Chem. Eur. J.* **2016**, *22*, 3304–3311; c) X.-Y. Liu, F. Zhang, T.-W. Goh, Y. Li, Y.-C. Shao, L. Luo, W. Huang, Y.-T. Long, L.-Y. Chou, C.-K. Tsung, *Angew. Chem. Int. Ed.* **2018**, *57*, 2110–2114.
[22] D. Saliba, M. Ammar, M. Rammal, M. Al-Ghoul, M. Hmadeh, *J. Am. Chem. Soc.* **2018**, *140*, 1812–1823.
[23] K. S. Park, Z. Ni, A. P. Côté, J. Y. Choi, R. Huang, F. J. Uribe-Romo, H. K. Chae, M. O'Keeffe, O. M. Yaghi, *Proc. Natl. Acad. Sci. USA* **2006**, *103*, 10186–10191.
[24] R. Banerjee, A. Phan, B. Wang, C. Knobler, H. Furukawa, M. O'Keeffe, O. M. Yaghi, *Science* **2008**, *319*, 939–943.
[25] a) M. He, J. Yao, Q. Liu, K. Wang, F. Chen, H. Wang, *Microporous Mesoporous Mater.* **2014**, *184*, 55–60; b) Y. Zhang, Y. Jia, *RSC Adv.* **2018**, *8*, 31471–31477.
[26] D. Zou, D. Liu, J. Zhang, *Energy Environ. Mater.* **2018**, *1*, 209–220.
[27] a) M. Zhao, J. Chen, B. Chen, X. Zhang, Z. Shi, Z. Liu, Q. Ma, Y. Peng, C. Tan, X.-J. Wu, H. Zhang, *J. Am. Chem. Soc.* **2020**, *142*, 8953–8961; b) L. Zhang, S. Yuan, L. Feng, B. Guo, J.-S. Qin, B. Xu, C. Lollar, D. Sun, H.-C. Zhou, *Angew. Chem. Int. Ed.* **2018**, *57*, 5095–5099.
[28] G. Kumari, K. Jayaramulu, T. K. Maji, C. Narayana, *J. Phys. Chem. A* **2013**, *117*, 11006–11012.
[29] V. Giannini, Y. Zhang, M. Forcales, J. G. Rivas, *Opt. Express* **2008**, *16*, 19674–19685.
[30] a) S. Schlücker, *Angew. Chem. Int. Ed.* **2014**, *53*, 4756–4795; b) J. Langer, D. Jimenez de Aberasturi, J. Aizpurua, R. A. Alvarez-Puebla, B. Auguié, J. J. Baumberg, G. C. Bazan, S. E. J. Bell, A. Boisen, A. G. Brolo, J. Choo, D. Cialla-May, V. Deckert, L. Fabris, K. Faulds, F. J. García de Abajo, R. Goodacre, D. Graham, A. J. Haes, C. L. Haynes, C. Huck, T. Itoh, M. Käll, J. Kneipp, N. A. Kotov, H. Kuang, E. C. Le Ru, H. K. Lee, J.-F. Li, X. Y. Ling, S. A. Maier, T. Mayerhöfer, M. Moskovits, K. Murakoshi, J.-M. Nam, S. Nie, Y. Ozaki, I. Pastoriza-Santos, J. Perez-Juste, J. Popp, A. Pucci, S. Reich, B. Ren, G. C. Schatz, T. Shegai, S. Schlücker, L.-L. Tay, K. G. Thomas, Z.-Q. Tian, R. P. Van Duyne, T. Vo-Dinh, Y. Wang, K. A. Willets, C. Xu, H. Xu, Y. Xu, Y. S. Yamamoto, B. Zhao, L. M. Liz-Marzán, *ACS Nano* **2020**, *14*, 28–117.
[31] R. A. Alvarez-Puebla, D. S. Dos Santos Jr, R. F. Aroca, *Analyst* **2004**, *129*, 1251–1256.
[32] a) W. Xie, C. Herrmann, K. Kömpe, M. Haase, S. Schlücker, *J. Am. Chem. Soc.* **2011**, *133*, 19302–19305; b) H. Zhang, X.-G. Zhang, J. Wei, C. Wang, S. Chen, H.-L. Sun, Y.-H. Wang, B.-H. Chen, Z.-L. Yang, D.-Y. Wu, J.-F. Li, Z.-Q. Tian, *J. Am. Chem. Soc.* **2017**, *139*, 10339–10346.
[33] a) X. Qiao, B. Su, C. Liu, Q. Song, D. Luo, G. Mo, T. Wang, *Adv. Mater.* **2018**, *30*, 1702275; b) H. Y. F. Sim, H. K. Lee, X. Han, C. S. L. Koh, G. C. Phan-Quang, C. L. Lay, Y. C. Kao, I. Y. Phang, E. K. L. Yeow, X. Y. Ling, *Angew. Chem. Int. Ed.* **2018**, *57*, 17058–17062.
[34] A. Mariño-Lopez, A. Sousa-Castillo, M. Blanco-Formoso, L. N. Furini, L. Rodríguez-Lorenzo, N. Pazos-Perez, L. Guerrini, M. Pérez-Lorenzo, M. A. Correa-Duarte, R. A. Alvarez-Puebla, *ChemNanoMat* **2019**, *5*, 46–50.
[35] A. Tripathi, E. D. Emmons, S. D. Christesen, A. W. Fountain III, J. A. Guicheteau, *J. Phys. Chem. C* **2013**, *117*, 22834–22842.
[36] R. Kumar, A. F. Ismail, *J. Appl. Polym. Sci.* **2015**, *132*, 42042.
[37] S. Xu, P. Chen, X. Lin, I. M. Khan, X. Ma, Z. Wang, *Anal. Chim. Acta* **2023**, *1240*, 340776.
[38] M. A. Correa-Duarte, N. Pazos Perez, L. Guerrini, V. Giannini, R. A. Alvarez-Puebla, *J. Phys. Chem. Lett.* **2015**, *6*, 868–874.
[39] Y.-F. Huang, H.-P. Zhu, G.-K. Liu, D.-Y. Wu, B. Ren, Z.-Q. Tian, *J. Am. Chem. Soc.* **2010**, *132*, 9244–9246.

Manuscript received: April 14, 2023
Accepted manuscript online: April 25, 2023
Version of record online: ■■, ■■

Research Articles

Nanostructures

T. Zorlu, I. B. Becerril-Castro, B. Puertolas, V. Giannini, M. A. Correa-Duarte,* R. A. Alvarez-Puebla* _____ **e202305299**

Yolk-Shell Nanostars@Metal Organic Frameworks as Molecular Sieves for Optical Sensing and Catalysis

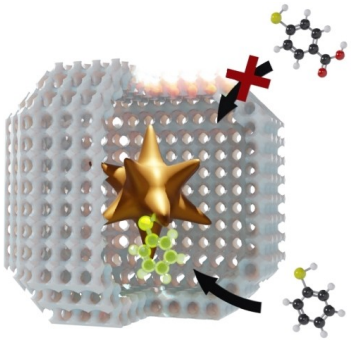

Homogeneous yolk shells consisting of a plasmonic gold nanostar coated with a metal–organic framework (MOF) were prepared. This configuration shows improved colloidal stability, can sieve different molecules based on their size or charge, displays interesting synergy with gold for application in photocatalysis and presents a strong optical activity for use as SERS sensors.